Magnetic lock-in transition and competing interactions in EuAuBi

S. H. Moody [1,*] C. Ritter [2] H. Takahashi [3,4] S. Ishiwata [3,4] and J. S. White [1,†]

[1]*Laboratory for Neutron Scattering and Imaging (LNS), PSI Center for Neutron and Muon Science, Paul Scherrer Institut (PSI), CH-5232 Villigen, Switzerland*

[2]*Institut Laue-Langevin, 38042 Grenoble Cedex 9, France*

[3]*Division of Materials Physics and Center for Spintronics Research Network (CSRN), Graduate School of Engineering Science, Osaka University, Osaka 560-8531, Japan*

[4]*Spintronics Research Network Division, Institute for Open and Transdisciplinary Research Initiatives, Osaka University, Yamadaoka 2-1, Suita, Osaka 565-0871, Japan*

(Received 7 March 2026; accepted 21 May 2026; published 9 July 2026)

The zero-field magnetic ground state of the superconducting polar semimetal EuAuBi is determined using neutron powder diffraction. The system realizes a commensurate antiferromagnetic ground state of wave vector $\mathbf{k} = (1/3, 0, 0)$ with moments along the crystallographic b axis and unequal moment amplitudes between the two magnetically inequivalent Eu orbits. On warming above an intermediate transition temperature, $T_{N2} \approx 3.3\,\mathrm{K}$, a commensurate-incommensurate transition occurs with $\mathbf{k}(T) = [1/3 - \delta(T), 0, 0]$, preserving the moment direction and occurring only within a narrow temperature window below the incommensurate-paramagnetic transition at $T_{N1} \approx 4\,\mathrm{K}$. A minimal isotropic exchange toy model including interactions up to third-nearest neighbors suggests the presence of competing interactions. Together, these results provide a foundation for future studies of materials hosting an interplay between magnetism, superconductivity, and electric polarity.

DOI: 10.1103/dp5g-fbpc

I. INTRODUCTION

Topological phenomena flavor electronic states with geometric properties that manifest as technologically utilizable quantized and anomalous responses within transport and spectroscopy [1–4]. In momentum space, symmetry-protected band crossings in Dirac and Weyl semimetals generate unusual magnetotransport signatures [5–9]. In real space, chiral magnets support topologically nontrivial spin textures such as magnetic skyrmions that exhibit emergent electrodynamics [10–12]. Combining these ingredients together with unconventional superconductivity [13–16] has strong potential to give rise to exotic collective phenomena. Identifying materials and studying the collective properties that lie at the intersection between these three cornerstones comprising topological condensed matter presents a novel frontier in physics.

The ABC-type ternary series of intermetallics provides a platform for exploring such an intersection. The series separates into different symmetry groups that host diverse correlated phenomena. For instance, in LiGaGe-type structures with $P6_3mc$ symmetry, buckled interstitial layers produce an electric polarity along the crystallographic c axis and theoretically are proposed as candidates for Rashba semiconductors and Dirac or Weyl semimetals [17–19]. In nonbuckled $P6/mmm$ AlB_2 systems, there exists a diverse range of correlated phenomena, including superconductivity in MgB_2 and topological noncoplanar incommensurate textures called magnetic skyrmions in frustrated triangular-lattice compounds such as Gd_2PdSi_3 [20–28]. These examples highlight the potential of these materials for realizing systems that combine nontrivial electronic topology, frustrated/topological magnetism, and superconductivity.

With this in mind, we identify EuAuBi as a candidate system. The material crystallizes with a polar hexagonal structure [Figs. 1(a) and 1(b)] in which Eu ions form a triangular lattice (alongside other materials such as $EuZn_2As_2$ [29], $EuSn_2As_2$ [30], EuAuAs [31], $EuAg_4Sb_2$ [32], and $EuCd_2As_2$ [33,34]), and the Au–Bi layers form a buckled honeycomb network [35,36]. Previous first-principles calculations have predicted Dirac-like band crossings near the Fermi level, and experiments have shown that surface-like superconductivity emerges at low temperatures [37]. The phase diagram is highly anisotropic, with the superconductivity persisting to relatively high fields for $H \parallel c$ compared to $H \parallel ab$, and the latter direction showing numerous metamagnetic transitions that are concomitant with the superconductivity as shown in Figs. 1(c) and 1(d).

Despite the potential of simultaneously hosting superconductivity and a nonvanishing electric polarization together with complex magnetic textures, the magnetic structure of EuAuBi has not been determined, nor has the possibility of

*Contact author: samuel.moody@psi.ch
†Contact author: jonathan.white@psi.ch

Published by the American Physical Society under the terms of the Creative Commons Attribution 4.0 International license. Further distribution of this work must maintain attribution to the author(s) and the published article's title, journal citation, and DOI.

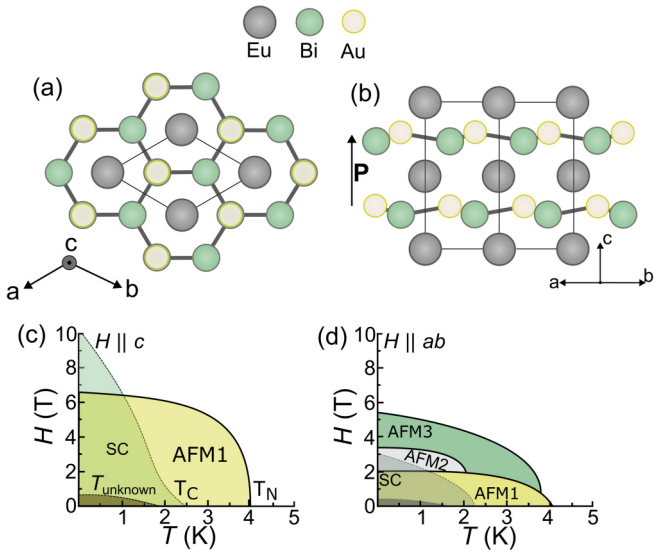

FIG. 1. (a), (b) Atomic crystal structure of EuAuBi viewed parallel and perpendicular to the c axis. Eu, Bi, and Au atoms are shown in gray, green, and yellow. (c), (d) Magnetic and superconducting phase diagrams as a function of temperature (T) and magnetic field (H) for $H \parallel \mathbf{c}$ and $H \perp \mathbf{c}$, constructed from data reported in Ref. [37]. In zero field, the AFM1 phase exhibits a reported double transition at $T_{N2} = 3.3\,\mathrm{K}$ and $T_{N1} = 4\,\mathrm{K}$, identified from heat capacity [37].

topologically nontrivial incommensurate phases been evaluated. Furthermore, in addition to magnetic-field-induced transitions, the zero-field temperature-dependent behavior is also rich, with heat-capacity measurements indicating a double magnetic transition at $T_{N1} \approx 4\,\mathrm{K}$ and $T_{N2} \approx 3.3\,\mathrm{K}$ [37]. Establishing the magnetic ground state and identifying whether the ground state is commensurate or incommensurate with the underlying crystal structure provides key insights into the likelihood of realizing a nontrivial magnetic topology.

Here, we bridge this gap and report neutron powder diffraction measurements that determine the magnetic ordering in EuAuBi. At the lowest temperatures, we find a commensurate magnetic structure with propagation vector $\mathbf{k} = (1/3, 0, 0)$ that evolves into an incommensurate state above an intermediate transition temperature T_{N2}. Together with magnetic space-group analysis, refinements of the neutron powder diffraction data show that the system realizes an antiferromagnetic structure with moments along b, where unequal moment amplitudes on the two Eu orbits account for weak reflections. A minimal toy model suggests that stabilizing this state requires competing exchange interactions, while anisotropic terms are likely needed to lock in the observed commensurate order. These results establish EuAuBi as a triangular-lattice magnet hosting both commensurate and incommensurate phases.

II. METHODS

Single crystals of EuAuBi were grown using a Bi self-flux method and subsequently ground into powder. High-purity Eu (99.9%), Au (99.99%), and Bi (99.999%) were combined in a molar ratio Eu:Au:Bi = 1:1:10 inside an Ar-filled glove box and loaded into an alumina crucible. The crucible was sealed in an evacuated quartz ampoule, heated to 1100 °C for 10 h, and then cooled to 400 °C at 4 °C h^{-1}. Excess Bi flux was removed by centrifugation. Room-temperature structural characterization was performed using powder x-ray diffraction on a Bruker D8 diffractometer with Cu Kα radiation. The diffraction pattern was indexed in space group $P6_3mc$ with lattice parameters $a = 4.8068(6)$ Å and $c = 8.2955(12)$ Å, with a minor Bi impurity phase from residual flux. Further growth details are given in Ref. [37].

Neutron powder diffraction measurements were carried out on the high-intensity two-axis diffractometer D20 at the Institut Laue-Langevin [38]. To mitigate the large neutron absorption cross section of natural europium, the powder sample was loaded into a custom double-walled annular copper container to minimize absorption effects. Approximately 1 g of EuAuBi powder was handled in a He glove box and pressurized to 10 bar to ensure good thermal contact at low temperatures. Measurements were performed using the 90° take-off angle option of D20 with a Ge(117) monochromator giving a short wavelength of $\lambda = 1.12$ Å to further reduce absorption effects while still providing a resolution sufficient to resolve closely spaced low-angle peaks associated with magnetic scattering.

The magnetic propagation vector was determined using the k-search utility in the FULLPROF SUITE [39]. Rietveld refinements of the nuclear structure were performed together with a Le Bail phase to account for preferred orientation effects in the sample container. Magnetic symmetry analysis and refinements were carried out using MAG2POL and the ISOTROPY software suite [40,41]. All magnetic refinements were performed using instrumental peak-shape and resolution parameters appropriate for the Ge(117) configuration. Peak asymmetry at low angles was modeled using a geometrical correction, and the remaining absorption effects were included using the built-in MAG2POL absorption correction. This correction improves the relative intensity balance of the low-angle reflections while increasing the propagated statistical uncertainties associated with corrected intensities [42]. The magnetic space group was generated using ISODISTORT based on the irreducible representation that provided the best fit to the diffraction data.

III. RESULTS AND DISCUSSION

The paramagnetic neutron powder diffraction pattern at 6 K (Fig. 2) is dominated by reflections from the copper sample holder, which obscure the weaker peaks from the limited sample volume. Accurate structural refinement therefore requires Le Bail fitting of the Cu contributions to isolate the sample intensities. The remaining reflections are consistent with the expected hexagonal EuAuBi structure (space group $P6_3mc$, No. 186) with lattice parameters $a = b = 4.776(1)$ Å and $c = 8.197(9)$ Å. Minor impurity peaks were identified as Bi ($R\bar{3}m$) and ignored during the fitting process. Upon cooling to 2.85 K, additional Bragg reflections emerge (inset), signaling the onset of long-range magnetic order. These peaks index with propagation vector $\mathbf{k} = (1/3, 0, 0)$, indicating a commensurate antiferromagnetic state that triples the crystallographic unit cell.

Magnetic symmetry analysis reduces the number of free parameters required to model the ordered state. For a generic

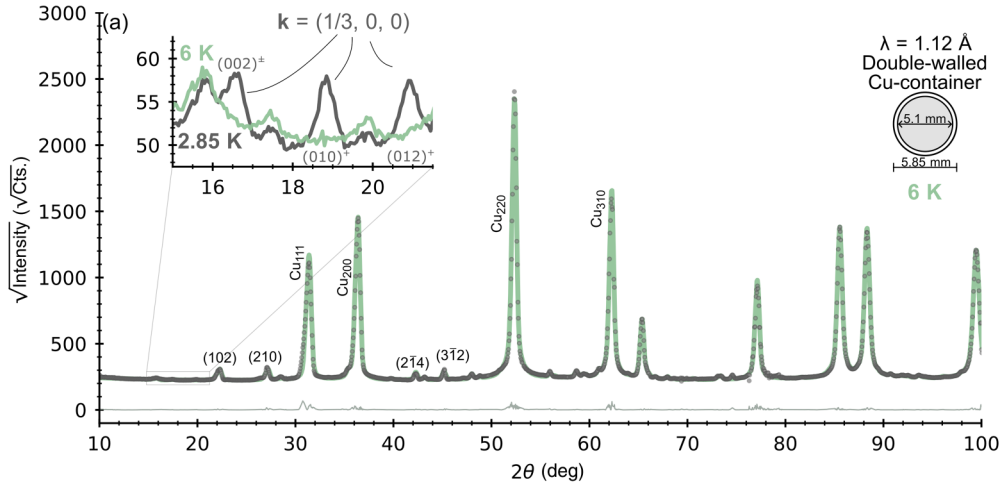

FIG. 2. Neutron powder diffraction pattern of EuAuBi at 6 K, plotted on a square-root y axis to enhance the visibility of the weaker sample peaks relative to the dominating copper container. Experimental data is shown as gray markers and the Rietveld refinement of the crystal structure as a green line. Inset shows both the 6 K dataset (green) and the 2.85 K dataset (gray), with the latter displaying new magnetic peaks indexed relative to the corresponding nuclear Bragg reflections as $(hkl)^{\pm}$, indicating additions or subtractions of the magnetic wave vector, k=(1/3, 0, 0). Also shown is a scale version of the double-walled sample container used to reduce absorption effects.

propagation vector along the crystallographic a direction, $\mathbf{k} = (q_x, 0, 0)$, the little group yields two irreducible representations, Γ_1 and Γ_2, and splits the Eu sites into two magnetically inequivalent positions: Eu-1 at (0,0,0.743) and Eu-2 at (0,0,0.243). These symmetry considerations apply irrespective of whether q_x is commensurate or incommensurate, provided $q_x \neq 0$. The Γ_1 representation contains a single basis vector, constraining the moments to lie along the b direction, $\phi_1 = (0, -1, 0)$. In contrast, Γ_2 comprises two basis vectors, $\phi_1 = (2, 1, 0)$ and $\phi_2 = (0, 0, 1)$, corresponding to components perpendicular to $\mathbf{k}$ and along the c axis, respectively.

The magnetic difference pattern (2.85–6 K) is shown in Fig. 3, where we compare refinements using each basis vector from each irreducible representation independently. In Fig. 3(a), refinement with the Γ_1 representation provides good overall agreement with the subtracted data. However, closer inspection shows that the model fails to reproduce the weak intensity observed at the (001) and (101) reflections, visible in the inset as a shoulder and a very weak peak at $2\theta = 9.6°$ and 13.1°, respectively. Allowing the two Eu orbit modes to refine independently is permitted by symmetry within the irreducible representation and introduces an imbalance in their magnitudes [7.85(4) μ_B and 4.1(1) μ_B]. Given the strong absorption corrections and limited absolute intensity calibration, we interpret these values primarily as relative mode amplitudes required by the diffraction intensities, rather than as an independent determination of absolute Eu moment magnitudes. Nonetheless, the inequivalence of the moment sizes between the two sites is characteristic of density-wave states arising in Ruderman-Kittel-Kasuya-Yosida (RKKY)-driven systems, with the magnetic structure corresponding to a multicomponent mode that can carry different amplitudes on different magnetic orbits [43,44].

The inequivalent mode amplitudes on the two Eu orbits account for the weak reflections otherwise forbidden using the single basis vector [Fig. 3(b)]. To test alternative models, we explored all linear combinations of the two irreducible representations and basis vectors, including complex mixing and relative phase offsets between the Eu sites. Refinements consistently yielded unstable solutions with large uncertainties and strong correlations in the covariance matrix. Specifically, refinements including the alternative irreducible representation, Γ_2, produce significantly poorer agreement: the first two reflections are absent in Fig. 3(c) for $\phi_1 = (2, 1, 0)$, while the fourth reflection is not reproduced in Fig. 3(d) for $\phi_2 = (0, 0, 1)$. Moreover, any linear combination of Γ_2 basis vectors systematically overestimates the weak $(1\bar{1}0)$ reflection. We therefore conclude that the magnetic structure is fully described by a single basis vector of the Γ_1 representation, and that the model shown in Fig. 3(b) provides the most consistent and physically minimal description of the data.

Using the identified irreducible representation within the ISODISTORT framework together with the parent space group, we explore possible symmetry-allowed magnetic space groups. Restricting the analysis to a single star of $\mathbf{k}$ yields three candidate magnetic space groups, of which only $Cmc2_1$ provides a satisfactory fit. The corresponding refinement is shown in Fig. 4. The quality of both the data and the model is highlighted in the inset of Fig. 4, which shows good agreement even at large scattering angles where magnetic intensity is strongly suppressed by the falling-off of the Eu^{2+} form factor. A real-space representation of the resulting magnetic structure is presented in Fig. 5, illustrating the unequal ordered moments on the two Eu sites and the threefold repetition of the magnetic unit cell along a. The ordered moments are constrained along b, with ferromagnetic coupling between sites related along both b and c. This magnetic space group is distinct from the Eu-triangular lattices mentioned previously [29–34].

During refinement, the global phase of the magnetic modulation is undetermined, as expected since diffraction is insensitive to an overall phase factor of the spin-density wave. We note that regardless of the phase, an equal-moment solution cannot be obtained within a model based on a single

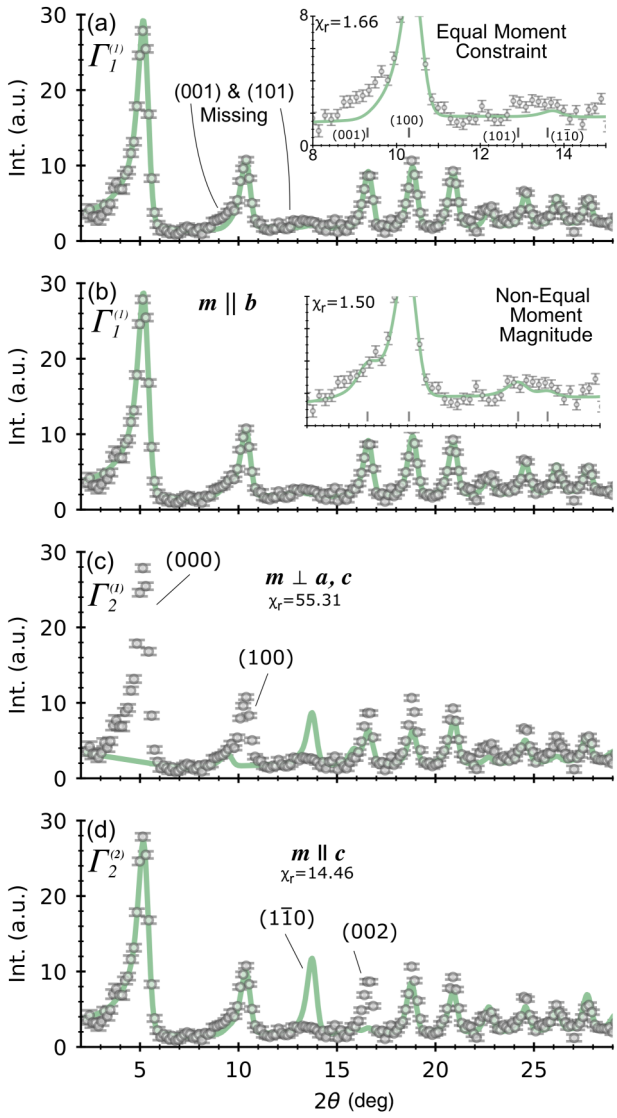

FIG. 3. Gray markers show the magnetic diffraction pattern obtained by subtracting the 6 K dataset from 2.85 K. (a) Fits to a magnetic structure using the Γ_1 IR with an additional constraint of equalizing the mode amplitude on both Eu sites. (b) As above but lifting the constraint as allowed by symmetry. Insets show the subtle improvements to the fit by breaking the equal-moment constraint. (c), (d) Fits to the second Γ_2 IR using each basis vector separately. See labels for moment direction. Indexed peaks omit the additional magnetic wave-vector notation, e.g., $(000) = (000) + k$.

irreducible representation and/or a single harmonic of **k**. No evidence for higher-order harmonics is observed in the diffraction data.

We next examine the temperature evolution of the magnetic phase. A Roots pump was installed on the cryostat, enabling measurements down to 1.44 K, below the reported superconducting transition. Diffraction data were collected on warming with 2-h scans up to 3.96 K, just below T_{N1}, and are shown in Fig. 6. Upon increasing temperature [Fig. 6(a)], the diffracted intensity decreases, as expected due to the reduction in magnetization with temperature. At the highest temperatures, the peaks remain well defined and do not exhibit any splitting. However, a slight shift in position is observed for some reflections toward the highest temperatures. In the absence of peak splitting, which would be expected for a doubly incommensurate structure of the form $\mathbf{k} = (a, b, 0)$, we model the magnetic structure using a one-dimensional propagation vector $\mathbf{k}(T) = [1/3 - \delta(T), 0, 0]$. We cannot exclude transverse components of **k** below the powder-resolution limit, though note that no splitting or additional reflections requiring such components are resolved. This model preserves the irreducible representation of the commensurate case, allowing for sequential refinements across all temperatures which only vary the moment magnitudes, propagation vector, background, and a broadening parameter.

As shown in Fig. 6(b), the ordered Eu moments evolve smoothly with temperature, with no anomalies indicative of additional phase transitions. Furthermore, the ratio of the ordered moments on the two Eu sites remains constant, implying that the magnetic structure does not undergo any directional rearrangement.

A temperature-driven magnetic phase transition is evident in Fig. 6(c), showing a lock-in transition from a commensurate state to an incommensurate phase with propagation vector $\mathbf{k}(T) = [1/3 - \delta(T), 0, 0]$ above the second transition temperature T_{N2}. The temperature dependence of $\delta(T)$ is smooth and continuous but does not follow the classical soliton-lattice form found for many commensurate-incommensurate transitions [45–49]. Instead, $\delta(T)$ grows nonlinearly on approaching T_{N1}, suggesting a thermally assisted mechanism similar to $TbNi_5$ [50–53]. In this picture, increasing temperature weakens the effective magnetic anisotropy that stabilizes the commensurate state, allowing the propagation vector to relax toward the minimum of the exchange interaction in continuum momentum space. Such behavior is consistent with a scenario in which the ordering wave vector is primarily selected by the RKKY-driven susceptibility, while the lower-temperature lock-in arises from competing single-ion or exchange anisotropies that energetically pin commensurate values [54].

This interpretation is further supported by heat-capacity data [37], which exhibit a secondary anomaly associated with additional entropy release at the onset of the incommensurate phase. The incommensurate state exists only within a narrow temperature window near the critical region and is accompanied by pronounced Gaussian broadening of magnetic Bragg peaks, indicative of significantly reduced magnetic correlation lengths compared to the low-temperature commensurate phase. We find no resolvable anomalies in the magnetic structure parameters near the reported superconducting transition, suggesting that the magnetic order is weakly coupled to superconductivity in the bulk. Any coupling is therefore likely subtle, and the superconductivity may be restricted to surface-related effects rather than bulk coexistence.

The transition into an incommensurate magnetic phase requires the magnetic structure to be described by magnetic superspace groups (MSSGs) [55]. Using ISODISTORT with an incommensurate propagation vector and the Γ_1 irreducible representation, we generated two candidate MSSGs. Refinements based on these candidates were inconclusive: the groups $A2_1ma.1'(0, 0, g)000s$ and $Bm.1'(a, b, 0)0s$ are indistinguishable within experimental uncertainty, reflecting

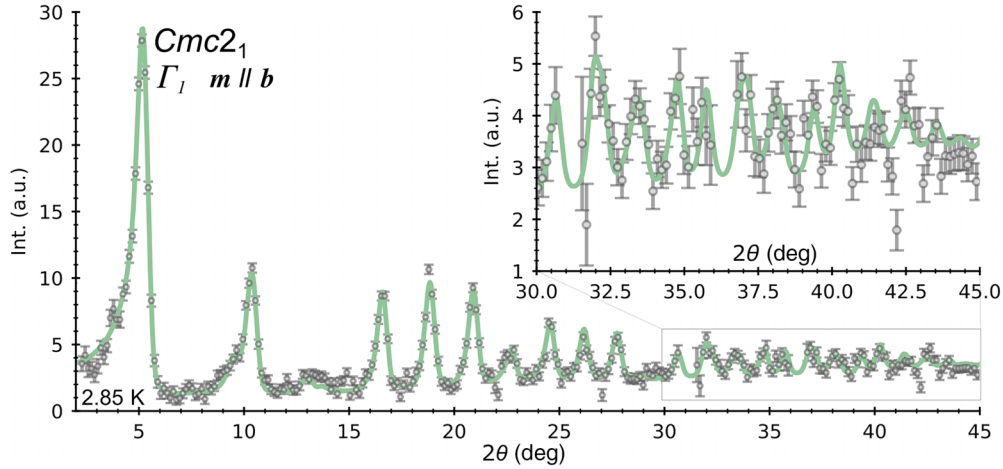

FIG. 4. Gray markers show the magnetic neutron diffraction pattern obtained by subtracting the paramagnetic dataset collected at 6 K from the dataset at 2.85 K. Green line shows a high-accuracy fit to the data of the $Cmc2_1$ magnetic space group, even at high scattering angles, as shown in the inset.

the limited magnetic scattering intensity near the transition temperature. Both MSSGs contain a mirror symmetry and a time-reversal-symmetric sinusoidal magnetic modulation. The orthorhombic $A2_1ma$ case additionally includes a 2_1 screw axis and a glide plane, giving it higher symmetry than the monoclinic Bm case. MSSGs that include a c-axis canting component derived from the Γ_2 representation are incompatible with the data, consistent with the considerations discussed above.

We now turn to the microscopic origin of the magnetic ground state. The system realizes a triangular lattice with propagation vector $\mathbf{k} = (1/3, 0, 0)$ (trailing zeros to be dropped hereafter) and ordered moments constrained along the crystallographic b direction. Isotropic Heisenberg models on the triangular lattice have been extensively studied in the context of quantum magnetism [56], where antiferromagnetic nearest-neighbor exchange stabilizes the well-known 120° structure [57,58]. A variety of other ordered and incommensurate states can also arise once further-neighbor interactions or anisotropies are introduced.

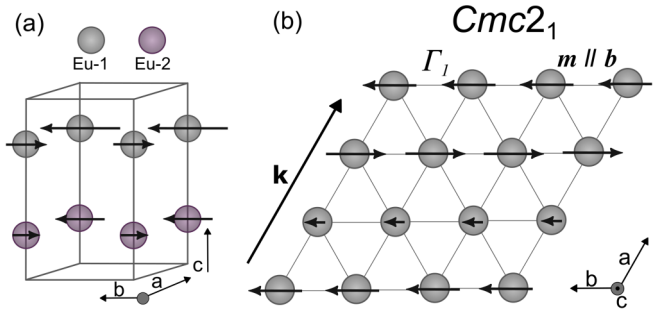

FIG. 5. Cartoon of the magnetic structure refined using the $Cmc2_1$ magnetic space group shown previously. (a) Two inequivalent Eu sites are aligned along the c direction with nonequal moment contributions as allowed by the space group symmetry. The moments are ferromagnetically coupled along the b and c axes. (b) View along the c axis showing the $\mathbf{k} \neq (1/3, 0, 0)$ modulation.

Our collinear $k = 1/3$ state with a fixed moment direction is not generically stabilized within such minimal models, indicating that additional interactions beyond simple isotropic nearest-neighbor exchange are relevant. These may include further-neighbor exchange, anisotropic exchange, or bond-dependent interactions analogous to Kitaev physics [59]. To gain insight into whether the system hosts competing interactions capable of stabilizing such an ordering wave vector, we consider a minimal classical Hamiltonian including interactions up to third neighbors,

$$H = \sum_{\langle ij\rangle_N} J_1\, \mathbf{S}_i \cdot \mathbf{S}_j + \sum_{\langle ij\rangle_{NN}} J_2\, \mathbf{S}_i \cdot \mathbf{S}_j + \sum_{\langle ij\rangle_{NNN}} J_3\, \mathbf{S}_i \cdot \mathbf{S}_j. \quad (1)$$

J_{1-3} denote the exchange interactions between nearest-, next-nearest-, and third-nearest-neighbor spins $\mathbf{S}_i$ and $\mathbf{S}_j$. Using Eq. (1), we evaluate the classical energies of four candidate states on the triangular lattice [AFM1–3 and FM, Fig. 7(a)], including the experimentally observed $k = 1/3$ configuration (AFM3). The resulting phase diagrams for both antiferromagnetic and ferromagnetic J_1 are presented in Figs. 7(b) and 7(c).

We find that the AFM3 ($k = 1/3$) state is stabilized when J_1, J_2, and J_3 are comparable in magnitude, placing the system within a setting of competing, and potentially frustrated interactions. The proximity of the AFM3 phase boundary to the incommensurate state (AFM1) indicates that the exchange parameters in our material may lie close to the phase competition line, potentially explaining the experimentally observed commensurate-incommensurate transition with increasing temperature.

We emphasize that anisotropic exchange and single-ion anisotropy terms are not included in this minimal treatment, which limits the scope of the toy model. Incorporating these contributions would enable a full minimization of the Hamiltonian and a quantitative comparison with experiment. However, determining them reliably requires inelastic neutron scattering measurements on isotopically enriched samples and detailed modeling, which lie beyond the scope of the present work. Nevertheless, the model indicates that the interactions

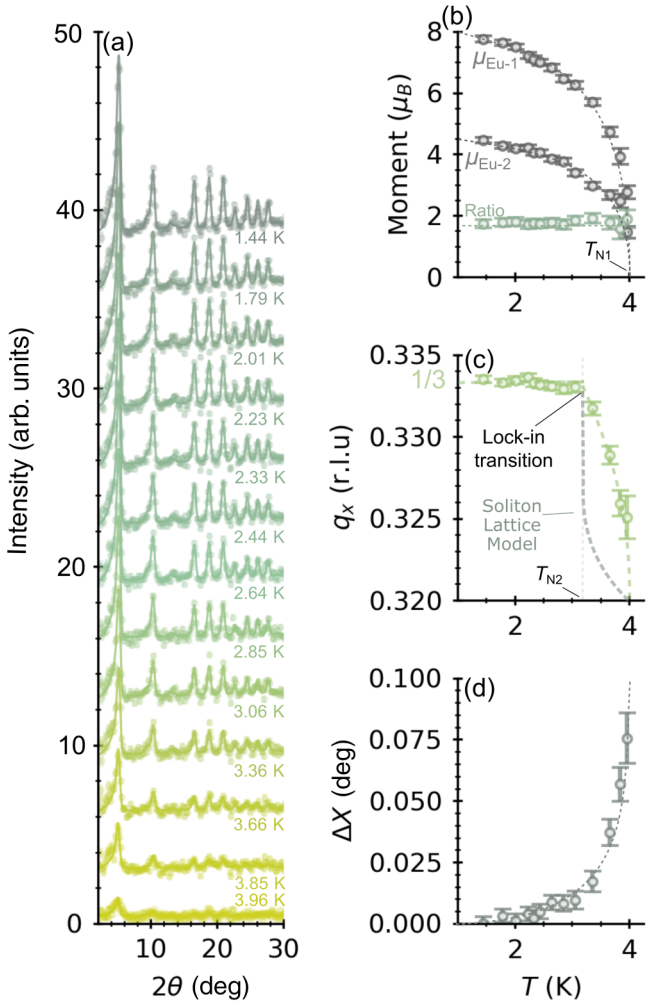

FIG. 6. Temperature dependence of the magnetic scattering intensity. (a) Rietveld refinements (lines) to the experimental data (markers) demonstrate excellent agreement across all measured temperatures. (b) Temperature dependence of the ordered moment on the Eu-1 and Eu-2 crystallographic sites; a constant ratio between the two sites (green markers) is maintained at all temperatures. (c) Evolution of the magnetic propagation vector with increasing temperature, changing from a commensurate state ($k = 1/3$) to an incommensurate state $\mathbf{k}(T) = [1/3 - \delta(T), 0, 0]$ upon crossing the T_{N2} transition. (d) The Gaussian broadening term in the peak-shape function increases strongly on approaching the magnetic ordering temperature, indicating a reduction of the magnetic correlation length.

reside in a competing regime, with our incommensurate and commensurate states lying adjacent to one another within the phase diagram.

The presence of competing exchange interactions raises the possibility of field-induced nontrivial spin textures. Although a commensurate $k = 1/3$ ground state disfavors skyrmion formation, frustrated triangular-lattice systems are known to host skyrmionic phases [60,61]. Moreover, the experimentally observed lock-in transition closely parallels the behavior reported in GaVS-type Néel-skyrmion materials [62–64], where

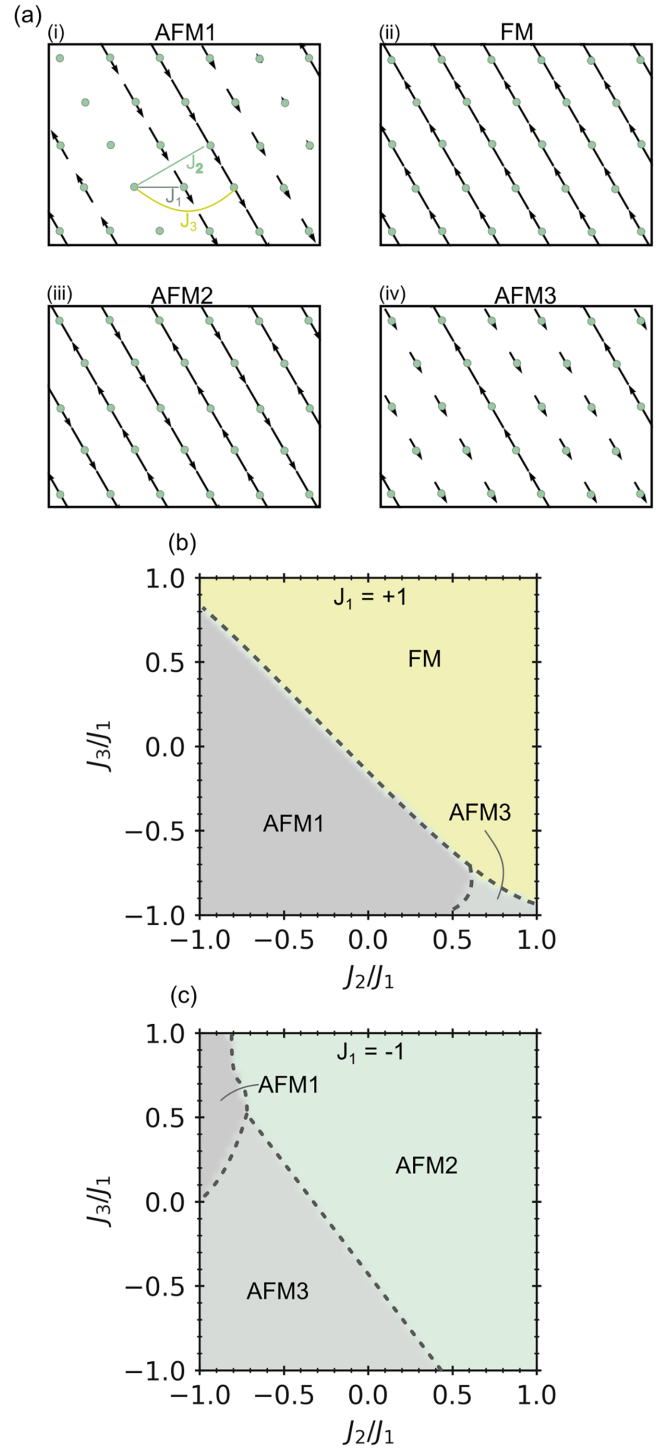

FIG. 7. Modeling the exchange interactions in EuAuBi. (a) Trial magnetic states used to generate the magnetic phase diagram, all satisfying the $\mathbf{m} \parallel b$ constraint imposed by the Γ_1 irreducible representation: (i) incommensurate AFM state with $k = 0.24$, (ii) ferromagnetic state with $k = 0$, (iii) commensurate AFM state with $k = 1/2$, and (iv) commensurate AFM state with $k = 1/3$, as observed in NPD. (b), (c) Magnetic phase diagrams showing the lowest-energy trial state as a function of next-nearest- and third-nearest-neighbor exchange (J_2 and J_3) for $J_1 > 0$ (b) and $J_1 < 0$ (c).

an incommensurate cycloidal state similarly emerges near the magnetic ordering temperature. Under applied magnetic field, these cycloids transform into a skyrmion lattice that remains stable only within a narrow temperature window close to T_N. At lower temperatures, both the skyrmion and cycloidal states collapse into a commensurate ferromagnetic phase, mirroring the sequence of competing commensurate and incommensurate states identified here. This analogy suggests that EuAuBi may lie close to an instability toward field-stabilized noncollinear or topological spin textures. This comparison does not establish skyrmion formation in EuAuBi, but motivates field-dependent single-crystal neutron diffraction or resonant x-ray scattering studies.

In summary, our neutron powder diffraction measurements on EuAuBi establish a commensurate $k = 1/3$ magnetic structure with inequivalent Eu moments and a narrow incommensurate regime near T_{N1}. The observed ordering is inconsistent with a simple nearest-neighbor Heisenberg model and instead points to substantial frustration arising from competing exchange interactions and anisotropic terms, placing this system in a competing regime conducive to complex field-induced spin textures with potentially emergent electronic responses.

ACKNOWLEDGMENTS

We are grateful to Peter Anderhuber and the mechanical workshop at the SINQ facility, PSI, Switzerland for manufacturing the copper sample container. The neutron experiments were performed at the Institut Laue Langevin, Grenoble, France, under Proposal No. 5-31-3061. This work was financially supported by the Swiss National Science Foundation Project No. 200021_188707, KAKENHI (Grants No. 23H04871, No. 24K00570, No. 25H00420, and No. 25H01248), FOREST (No. JPMJFR236K) from JST, and the Asahi Glass Foundation.

DATA AVAILABILITY

The data that support the findings of this article are openly available [65].

[1] É. Lantagne-Hurtubise and M. Franz, Topology in abundance, Nat. Rev. Phys. **1**, 183 (2019).
[2] M. G. Vergniory, L. Elcoro, C. Felser, N. Regnault, B. A. Bernevig, and Z. Wang, A complete catalogue of high-quality topological materials, Nature (London) **566**, 480 (2019).
[3] F. Tang, H. C. Po, A. Vishwanath, and X. Wan, Comprehensive search for topological materials using symmetry indicators, Nature (London) **566**, 486 (2019).
[4] T. Zhang, Y. Jiang, Z. Song, H. Huang, Y. He, Z. Fang, H. Weng, and C. Fang, Catalogue of topological electronic materials, Nature (London) **566**, 475 (2019).
[5] N. P. Armitage, E. J. Mele, and A. Vishwanath, Weyl and Dirac semimetals in three-dimensional solids, Rev. Mod. Phys. **90**, 015001 (2018).
[6] A. A. Burkov and L. Balents, Weyl semimetal in a topological insulator multilayer, Phys. Rev. Lett. **107**, 127205 (2011).
[7] X. Wan, A. M. Turner, A. Vishwanath, and S. Y. Savrasov, Topological semimetal and Fermi-arc surface states in the electronic structure of pyrochlore iridates, Phys. Rev. B **83**, 205101 (2011).
[8] S. M. Young, S. Zaheer, J. C. Y. Teo, C. L. Kane, E. J. Mele, and A. M. Rappe, Dirac semimetal in three dimensions, Phys. Rev. Lett. **108**, 140405 (2012).
[9] A. A. Burkov, Weyl metals, Annu. Rev. Condens. Matter Phys. **9**, 359 (2018).
[10] N. Nagaosa and Y. Tokura, Topological properties and dynamics of magnetic skyrmions, Nat. Nanotechnol. **8**, 899 (2013).
[11] A. Fert, V. Cros, and J. Sampaio, Skyrmions on the track, Nat. Nanotechnol. **8**, 152 (2013).
[12] S. Mühlbauer, B. Binz, F. Jonietz, C. Pfleiderer, A. Rosch, A. Neubauer, R. Georgii, and P. Böni, Skyrmion lattice in a chiral magnet, Science **323**, 915 (2009).
[13] M. R. Norman, The challenge of unconventional superconductivity, Science **332**, 196 (2011).
[14] G. Bednik, A. A. Zyuzin, and A. A. Burkov, Superconductivity in Weyl metals, Phys. Rev. B **92**, 035153 (2015).
[15] M. Sigrist and K. Ueda, Phenomenological theory of unconventional superconductivity, Rev. Mod. Phys. **63**, 239 (1991).
[16] M. Smidman, M. B. Salamon, H. Q. Yuan, and D. F. Agterberg, Superconductivity and spin–orbit coupling in noncentrosymmetric materials: A review, Rep. Prog. Phys. **80**, 036501 (2017).
[17] A. Narayan, Class of Rashba ferroelectrics in hexagonal semiconductors, Phys. Rev. B **92**, 220101(R) (2015).
[18] H. Gao, Y. Kim, J. W. F. Venderbos, C. L. Kane, E. J. Mele, A. M. Rappe, and W. Ren, Dirac-Weyl semimetal: Coexistence of Dirac and Weyl fermions in polar hexagonal ABC crystals, Phys. Rev. Lett. **121**, 106404 (2018).
[19] I. R. Shein, N. I. Medvedeva, and A. L. Ivanovskii, Band structure of new superconducting AlB_2-like ternary silicides $M(Al_{0.5}Si_{0.5})_2$ and $M(Ga_{0.5}Si_{0.5})_2$ (where M = Ca, Sr and Ba), J. Phys.: Condens. Matter **15**, L541 (2003).
[20] J. Nagamatsu, N. Nakagawa, T. Muranaka, Y. Zenitani, and J. Akimitsu, Superconductivity at 39 K in magnesium diboride, Nature (London) **410**, 63 (2001).
[21] D. I. Walicka, O. Blacque, T. Klimczuk, and F. O. von Rohr, From weak- to strong-coupling superconductivity in the AlB_2-type solid solution $SrGa_{1-x}Al_xGe$ with honeycomb layers, J. Phys.: Condens. Matter **37**, 045704 (2025).
[22] M. J. Evans, Y. Wu, V. F. Kranak, N. Newman, A. Reller, F. J. Garcia-Garcia, and U. Häussermann, Structural properties and superconductivity in the ternary intermetallic compounds MAB (M = Ca, Sr, Ba; A = Al, Ga, In; B = Si, Ge, Sn), Phys. Rev. B **80**, 064514 (2009).
[23] D. I. Walicka, O. Blacque, K. Gornicka, J. S. White, T. Klimczuk, and F. O. von Rohr, Magnetism in EuAlSi and the $Eu_{1-x}Sr_xAlSi$ solid solution, Phys. Rev. Res. **7**, 033126 (2025).
[24] V. H. Tran, M. Sahakyan, and Z. Bukowski, Discovery of superconductivity in AlB_2-type hexagonal YGa_2, J. Phys.: Condens. Matter **33**, 315401 (2021).
[25] T. Kurumaji, T. Nakajima, M. Hirschberger, A. Kikkawa, Y. Yamasaki, H. Sagayama, H. Nakao, Y. Taguchi, T.-H. Arima,

and Y. Tokura, Skyrmion lattice with a giant topological Hall effect in a frustrated triangular-lattice magnet, Science **365**, 914 (2019).

[26] J. A. M. Paddison, B. K. Rai, A. F. May, S. Calder, M. B. Stone, M. D. Frontzek, and A. D. Christianson, Magnetic interactions of the centrosymmetric skyrmion material Gd_2PdSi_3, Phys. Rev. Lett. **129**, 137202 (2022).

[27] M. Gomilšek, T. J. Hicken, M. N. Wilson, K. J. A. Franke, B. M. Huddart, A. Štefančič, S. J. R. Holt, G. Balakrishnan, D. A. Mayoh, M. T. Birch, S. H. Moody, H. Luetkens, Z. Guguchia, M. T. F. Telling, P. J. Baker, S. J. Clark, and T. Lancaster, Anisotropic skyrmion and multi-q spin dynamics in centrosymmetric Gd_2PdSi_3, Phys. Rev. Lett. **134**, 046702 (2025).

[28] S. H. Moody, P. J. Bereciartua, S. Francoual, M. T. Littlehales, M. N. Wilson, M. Gomilšek, M. T. Birch, D. A. Mayoh, G. Balakrishnan, and P. D. Hatton, Local Dzyaloshinskii-Moriya interactions driving quasi-2D magnetism in a centrosymmetric nanoskyrmion material, Phys. Rev. Lett. **135**, 076706 (2025).

[29] Z. Bukowski, D. Rybicki, M. Babij, J. Przewoźnik, Ł. Gondek, J. Żukrowski, and C. Kapusta, Canted antiferromagnetic order in $EuZn_2As_2$ single crystals, Sci. Rep. **12**, 14718 (2022).

[30] S. Pakhira, M. A. Tanatar, T. Heitmann, D. Vaknin, and D. C. Johnston, a-type antiferromagnetic order and magnetic phase diagram of the trigonal Eu spin-$\frac{7}{2}$ triangular-lattice compound $EuSn_2As_2$, Phys. Rev. B **104**, 174427 (2021).

[31] S. Malick, J. Singh, A. Laha, V. Kanchana, Z. Hossain, and D. Kaczorowski, Electronic structure and physical properties of EuAuAs single crystal, Phys. Rev. B **105**, 045103 (2022).

[32] S. Ma, C. Zheng, J. He, B. Liu, S. Jin, C. Ma, H. Liang, C. Liu, and H. Shi, Magnetic phase diagram of triangular lattice Eu-based compound $EuAg_4Sb_2$, J. Supercond. Novel Magn. **38**, 28 (2025).

[33] Y. Xu, L. Das, J. Z. Ma, C. J. Yi, S. M. Nie, Y. G. Shi, A. Tiwari, S. S. Tsirkin, T. Neupert, M. Medarde, M. Shi, J. Chang, and T. Shang, Unconventional transverse transport above and below the magnetic transition temperature in Weyl semimetal $EuCd_2As_2$, Phys. Rev. Lett. **126**, 076602 (2021).

[34] J.-Z. Ma, S. M. Nie, C. J. Yi, J. Jandke, T. Shang, M. Y. Yao, M. Naamneh, L. Q. Yan, Y. Sun, A. Chikina, V. N. Strocov, M. Medarde, M. Song, Y.-M. Xiong, G. Xu, W. Wulfhekel, J. Mesot, M. Reticcioli, C. Franchini, C. Mudry, *et al.*, Spin fluctuation induced Weyl semimetal state in the paramagnetic phase of $EuCd_2As_2$, Sci. Adv. **5**, eaaw4718 (2019).

[35] C. Tomuschat and H.-U. Schuster, ABX-verbindungen mit modifizierter Ni_2In-struktur, Z. Naturforsch. B **36**, 1193 (1981).

[36] C. Tomuschat and H.-U. Schuster, Magnetische eigenschaften der verbindungsreihe EuBX mit B = Element der ersten Neben- und X = Element der fünften Hauptgruppe, Z. Anorg. Allg. Chem. **518**, 161 (1984).

[37] H. Takahashi, K. Akiba, M. Takahashi, A. H. Mayo, M. Ochi, T. C. Kobayashi, and S. Ishiwata, Superconductivity in a magnetic Rashba semimetal EuAuBi, J. Phys. Soc. Jpn. **92**, 013701 (2023).

[38] T. C. Hansen, P. F. Henry, H. E. Fischer, J. Torregrossa, and P. Convert, The D20 instrument at the ILL: A versatile high-intensity two-axis neutron diffractometer, Meas. Sci. Technol. **19**, 034001 (2008).

[39] J. Rodríguez-Carvajal, Recent advances in magnetic structure determination by neutron powder diffraction, Physica B **192**, 55 (1993).

[40] N. Qureshi, *Mag2Pol*: A program for the analysis of spherical neutron polarimetry, flipping ratio and integrated intensity data, J. Appl. Crystallogr. **52**, 175 (2019).

[41] B. J. Campbell, H. T. Stokes, D. E. Tanner, and D. M. Hatch, ISODISPLACE: A web-based tool for exploring structural distortions, J. Appl. Cryst. **39**, 607 (2006).

[42] A. W. Hewat, Absorption corrections for neutron diffraction, Acta Crystallogr. Sect. A **35**, 248 (1979).

[43] J. Rossat-Mignod, P. Burlet, J. Villain, H. Bartholin, W. Tcheng-Si, D. Florence, and O. Vogt, Phase diagram and magnetic structures of CeSb, Phys. Rev. B **16**, 440 (1977).

[44] J. Jensen and A. Mackintosh, *Rare Earth Magnetism: Structures and Excitations*, International Series of Monographs on Physics (Clarendon Press, Oxford, 1991).

[45] A. D. Bruce, R. A. Cowley, and A. F. Murray, The theory of structurally incommensurate systems. II. Commensurate-incommensurate phase transitions, J. Phys. C **11**, 3591 (1978).

[46] T. Chattopadhyay, P. J. Brown, P. Thalmeier, and H. G. v. Schnering, Incommensurate magnetic phase in $EuAs_3$ with zone-boundary lock-in, Phys. Rev. Lett. **57**, 372 (1986).

[47] T. Chattopadhyay, K. D. Liss, and T. Brückel, Incommensurate-commensurate lock-in phase transition in $EuAs_3$, J. Magn. Magn. Mater. **177–181**, 1058 (1998).

[48] J. Gunasekera, L. Harriger, A. Dahal, A. Maurya, T. Heitmann, S. M. Disseler, A. Thamizhavel, S. Dhar, D. J. Singh, and D. K. Singh, Electronic nature of the lock-in magnetic transition in $Ce_xAl_4Si_2$, Phys. Rev. B **93**, 155151 (2016).

[49] J. S. Helton, Y. Chen, G. L. Bychkov, S. N. Barilo, N. Rogado, R. J. Cava, and J. W. Lynn, Evolution of the commensurate and incommensurate magnetic phases of the $S = 3/2$ kagome staircase $Co_3V_2O_8$ in an applied field, J. Phys.: Condens. Matter **24**, 016003 (2012).

[50] S. G. Bogdanov, E. G. Gerasimov, Y. N. Skryabin, E. A. Sherstobitova, V. V. Sikolenko, R. Schedler, and A. N. Pirogov, Commensurate-incommensurate magnetic phase transition induced in $TbNi_5$ by an external magnetic field, Phys. Met. Metall. **113**, 228 (2012).

[51] H. Lee, Y. N. Choi, A. N. Pirogov, V. A. Kazantsev, and E. G. Gerasimov, Magnetic lock-in phase transition in $Tb_{0.95}Er_{0.05}Ni_5$ driven by low magnetic fields, J. Magn. Magn. Mater. **341**, 129 (2013).

[52] S. Lee, A. N. Pirogov, A. A. Podlesnyak, K. Prokeš, Y. Dorofeef, A. E. Teplykh, I. P. Swainson, and J.-G. Park, Unusual magnetic phase transitions of $TbNi_5$, Physica B **385–386**, 349 (2006).

[53] D. Parshall, G. Chen, L. Pintschovius, D. Lamago, T. Wolf, L. Radzihovsky, and D. Reznik, Competition between commensurate and incommensurate magnetic ordering in $Fe_{1+y}Te$, Phys. Rev. B **85**, 140515(R) (2012).

[54] Y. A. Izyumov, Modulated, or long-periodic, magnetic structures of crystals, Sov. Phys. Usp. **27**, 845 (1984).

[55] A. Janner and T. Janssen, Symmetry of incommensurate crystal phases. II. Incommensurate basic structure, Acta Crystallogr. Sect. A **36**, 408 (1980).

[56] E. Rastelli, Spin waves in non-collinear systems, *Statistical Mechanics of Magnetic Excitations* (World Scientific, Singapore, 2013), pp. 188–240.

[57] P. W. Anderson, Ordering and antiferromagnetism in ferrites, Phys. Rev. **102**, 1008 (1956).

[58] H. Kawamura, Universality of phase transitions of frustrated antiferromagnets, J. Phys.: Condens. Matter **10**, 4707 (1998).

[59] M. Hermanns, I. Kimchi, and J. Knolle, Physics of the Kitaev model: Fractionalization, dynamic correlations, and material connections, Annu. Rev. Condens. Matter Phys. **9**, 17 (2018).

[60] A. O. Leonov and M. Mostovoy, Multiply periodic states and isolated skyrmions in an anisotropic frustrated magnet, Nat. Commun. **6**, 8275 (2015).

[61] S.-Z. Lin and S. Hayami, Ginzburg-Landau theory for skyrmions in inversion-symmetric magnets with competing interactions, Phys. Rev. B **93**, 064430 (2016).

[62] I. Kézsmárki, S. Bordács, P. Milde, E. Neuber, L. M. Eng, J. S. White, H. M. Rønnow, C. D. Dewhurst, M. Mochizuki, K. Yanai, H. Nakamura, D. Ehlers, V. Tsurkan, and A. Loidl, Néel-type skyrmion lattice with confined orientation in the polar magnetic semiconductor: GaV_4S_8, Nat. Mater. **14**, 1116 (2015).

[63] E. Ruff, S. Widmann, P. Lunkenheimer, V. Tsurkan, S. Bordács, I. Kézsmárki, and A. Loidl, Multiferroicity and skyrmions carrying electric polarization in GaV_4S_8, Sci. Adv. **1**, e1500916 (2015).

[64] J. S. White, A. Butykai, R. Cubitt, D. Honecker, C. D. Dewhurst, L. F. Kiss, V. Tsurkan, and S. Bordács, Direct evidence for cycloidal modulations in the thermal-fluctuation-stabilized spin spiral and skyrmion states of GaV_4S_8, Phys. Rev. B **97**, 020401(R) (2018).

[65] S. H. Moody, Dataset for Magnetic Lock-In Transition and Competing Interactions in EuAuBi, Zenodo, 2026, http://doi.org/10.5281/zenodo.20593005.